

Improved efficiency of high resolution thermal and cold neutron imaging

A. S. Tremsin^{a,*}, J. B. McPhate^a, J. V. Vallerga^a, O. H. W. Siegmund^a, W. B. Feller^b, E. Lehmann^c, M. Dawson^d

^aSpace Sciences Laboratory, University of California, Berkeley, CA 94720, USA

^bNOVA Scientific, Inc., 10 Picker Rd., Sturbridge, MA 01566, USA

^cPaul Scherrer Institute, CH-5232, Villigen, Switzerland

^dHelmholtz Centre Berlin for Materials and Energy, Germany

Abstract

Spatial resolution and detection efficiency of neutron imaging detectors are the crucial parameters defining the ultimate resolution in neutron radiography, micro-tomography and other nondestructive testing techniques. The most widely used neutron imaging systems use a neutron-sensitive scintillation screen lens coupled to a CCD or a CMOS sensor. The highest spatial resolution in those devices is achieved using very thin scintillation screens which reduce image blurring due to light spreading in the scintillator. Thus high spatial resolution and high detection efficiency usually could not be achieved in the same device. Neutron counting detectors using neutron-sensitive microchannel plates (MCPs) overcome that deficiency by providing a long neutron absorption path (~mm scale) and preserving events within a single sub-10 μm pore. At the same time, each neutron in those detectors can be time-tagged with ~1 μs accuracy. The latest boron-10 and gadolinium-doped MCPs developed by Nova Scientific were tested at the cold neutron facility ICON of Paul Scherrer Institute and proved to be capable of imaging cold neutrons with 70% detection efficiency. Neutron radiography and micro-tomography confirmed the high spatial resolution capabilities of the latest generation of high efficiency microchannel plates.

The high spatial and temporal resolution of our neutron counting detectors allows for high resolution micro-tomography, novel studies of material composition, texture, phase and strain through Bragg edge imaging as well as dynamic studies of magnetic fields inside of thick samples, exploiting the neutron spin interactions with magnetic fields.

Keywords: Neutron radiography, High resolution, Detection efficiency, Non-destructive testing

* Corresponding author. Tel.: +1-510-642-4554; fax: +1-510-643-9729; E-mail address: ast@ssl.berkeley.edu

1. Introduction

Both the spatial resolution of neutron imaging detectors and their quantum efficiency need to be maximized for high resolution applications. The intensity of the neutron beam and the number of detected neutrons in each pixel of the image determine the image acquisition time. High spatial resolution imaging, with pixels as small as ~20 μm together with the limited intensity of most neutron beam lines (~ 10^6 - 10^7 n/cm²/s [1]-[4]), mandate relatively long acquisition times in order to achieve adequate statistics of at least ~100 neutrons per pixel. That translates to image acquisition times on the order of 2.5 to 25 seconds, at an idealized detection efficiency of 100%. However, with a detection efficiency of an order of magnitude lower, 10%, acquisition times increase to 25-250 seconds, making a single tomographic acquisition with 360 projections take

as long as 2.5 to 25 hours. Thus the improvement of detection efficiency can reduce data acquisition times to acceptable levels, thus allowing several samples to be studied in high resolution mode within a single day. Moreover, the new energy-resolved imaging mode or the Bragg edge imaging techniques require acquisition of multiple images corresponding to different neutron energies [5]. The detection efficiency becomes critical and even more important in high resolution studies of texture and strain [6]-[8], where the neutron transmission spectra are to be built within each pixel of the image and therefore much greater numbers of neutrons need to be acquired. The previous generation of neutron-sensitive microchannel plates (built by Nova Scientific, Sturbridge, MA) doped with ¹⁰B atoms have shown detection efficiencies as high as 43% for cold neutrons and 18% for thermal neutrons [9], while our detailed modeling indicates that for an optimized MCP geometry with

realistic doping levels we could achieve efficiencies as high as 70% and 50% for cold and thermal neutrons, respectively [10].

2. Experimental setup

The most recent MCP proprietary glass composition developed by Nova Scientific was used in a new set of neutron-sensitive microchannel plates and was recently tested in our detector [11] with Timepix [12] readout (used in the event counting mode). The neutron detector was installed at the ICON cold neutron beam facility of Paul Scherrer Institute [4]. The neutron sensitive MCP with $\sim 9 \mu\text{m}$ pores and an L/D ratio of 105:1 was installed in direct contact with a chevron stack of 40:1 MCPs with $10 \mu\text{m}$ pores, with the latter being used for event amplification. The spectrum of the ICON beam line, peaking at $\sim 4.7 \text{ meV}$, is shown in Fig. 1. A 2-cm beam aperture was used during the measurements, resulting in an integrated beam intensity at the detector position of $8.4 \times 10^6 \text{ n/cm}^2/\text{s}$.

One of the unique features of our detection system is the nearly total absence of readout noise, which enables very accurate neutron counting within a precisely controlled acquisition frame, as shown in Fig. 2. Each spot on the images of Fig. 2 corresponds to an individual neutron. Upon absorption in the MCP microchannel walls each neutron creates reaction products by interacting with a ^{10}B or Gd atom. These charged particles (alpha or ^7Li nuclei in the case of ^{10}B , or conversion electrons in the case of Gd), escape into an adjacent pore and initiate development of an electron avalanche – which can then be registered as a strong charge pulse of $\sim 1 \text{ ns}$ pulse width.

3. Results and discussion

3.1 Neutron detection efficiency

The highly statistical nature of the electron amplification process within the MCP microchannel or pore, and the fact that neutrons can be absorbed anywhere in the bulk of the neutron-sensitive MCP, leads to some variation of the event gain, in turn leading to some variation of event footprint on the Timepix readout. Obviously, an increased value of the Timepix lower level threshold eliminates the low gain events and reduces the average size of the footprint down to $\sim 1\text{-}2$ pixels, as shown in Fig. 2.c. At the same time this reduces the detection efficiency, as some events fall below the threshold. An optimal setting for the spatial resolution and detection efficiency in our detector can be selected in software for each particular measurement, without any change in the detector hardware.

The measured neutron detection efficiency of this new

MCP detector is shown in Fig. 3 as a function of bias voltage applied to the MCP for three different values of the Timepix threshold, and with a noise floor observed at a threshold of ~ 325 . The number of spots in short acquisition images similar to Fig. 2, taken at different MCP voltages and Timepix thresholds, is equal to the number of detected neutrons. Knowing the incoming neutron flux, we calculate the detection efficiency from the ratio of detected events to the number of incoming neutrons. As can be seen in Fig. 3, an increase in MCP bias leads to higher detector gain, thus improving the detection efficiency until most events appear well above the Timepix threshold value. The latter explains why at a threshold of 0.5 ke^- , the detection efficiency does not increase with MCP bias values above 1150 V , but instead saturates. Fig. 4 shows the detection efficiency as a function of the Timepix threshold, while the average width of the event footprint is shown in Fig. 5. Obviously, the highest detection efficiency in the current detector, which uses a $500 \mu\text{m}$ gap between the MCP and the readout is achieved with relatively large $\sim 2 \times 2$ pixel wide spots, on average. The optimal detector configuration balancing detection efficiency and spatial resolution can be determined with the help of the data presented in Figs. 4 and 5.

3.2 Spatial resolution of neutron radiography and micro-tomography

We have used the neutron-sensitive MCP detector in neutron radiography and micro-tomography measurements, to verify their high spatial resolution capabilities. A non-optimized high Timepix threshold value of 7.1 ke^- was selected for those measurements, due simply to the lack of beam time. One of the concerns about the new MCP glass composition was due to the presence of Gd-doping, with the suggestion that it may possibly lead to a halo effect due to the presence of prompt gamma photons for each neutron capture reaction in Gd. The radiographic and micro-tomographic images shown in Figs. 6 and 7 confirm the high spatial resolution capability of the latest generation ^{10}B - and Gd-doped microchannel plates, with no such halo actually being observed.

4. Conclusion

The results of our measurements confirmed the predicted detection efficiency values of 70% for a cold neutron beam spectrum. The unique combination of this very high neutron detection efficiency, event localization within a single MCP pore ($< 10 \mu\text{m}$ in diameter), timing resolution of $\sim 1 \mu\text{s}$ and the virtual absence of readout noise in existing readout electronics, make these new MCP imaging neutron detectors highly attractive for a

number of applications, such as high-resolution radiography and micro-tomography, Bragg edge diffraction imaging in TOF (time-of-flight) mode, imaging of magnetic fields with polarized neutrons, and others. Although at the moment the active area of existing neutron-sensitive MCPs is limited to $\sim 3\text{-}4$ cm in diameter, this is already adequate for a number of high resolution applications. Considerably larger formats are currently being developed by Nova Scientific and will become available in time, as well as even higher neutron sensitivity through increased doping levels with neutron-absorbing atoms. We also plan to calibrate the detection efficiency for thermal neutrons in the near future.

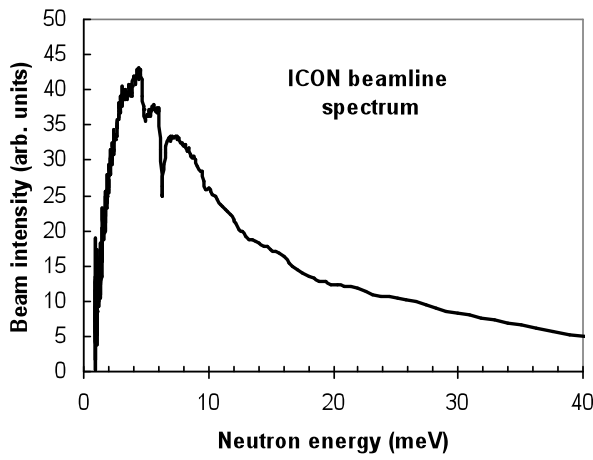


Fig. 1. The spectrum of the cold neutron beam line at the ICON facility of Paul Scherrer Institute where the detection efficiency of the MCP detector was measured. Peak neutron energy ~ 4.7 meV (4.17 Å).

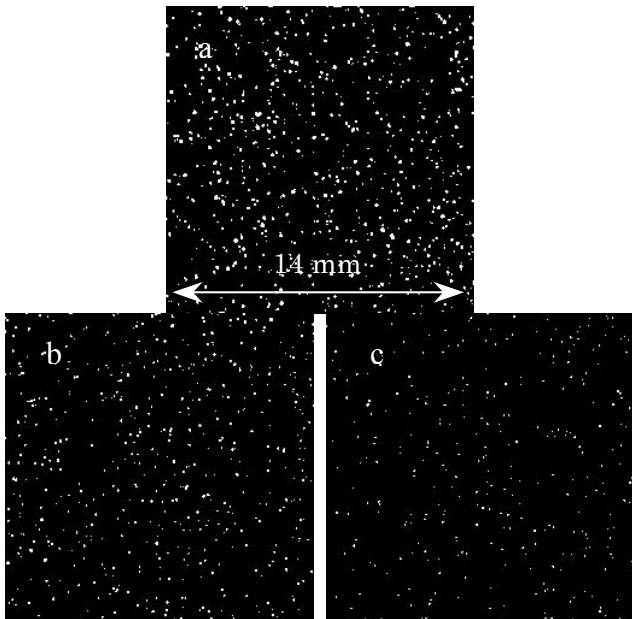


Fig. 2. Individual 100- μs acquisition frames measured at Timepix threshold levels of 335 (a), 400 (b) and 600 (c). Each spot in the image

corresponds to the detection of a single neutron. Distance between the MCP and the Timepix readout ~ 500 μm . Neutron sensitive MCP is biased at 1100V and the two amplification MCPs are biased at 550V each. The presence of a pulse height distribution in the MCP output results in a spread of the event footprint size, which can be reduced by a smaller MCP-Timepix distance.

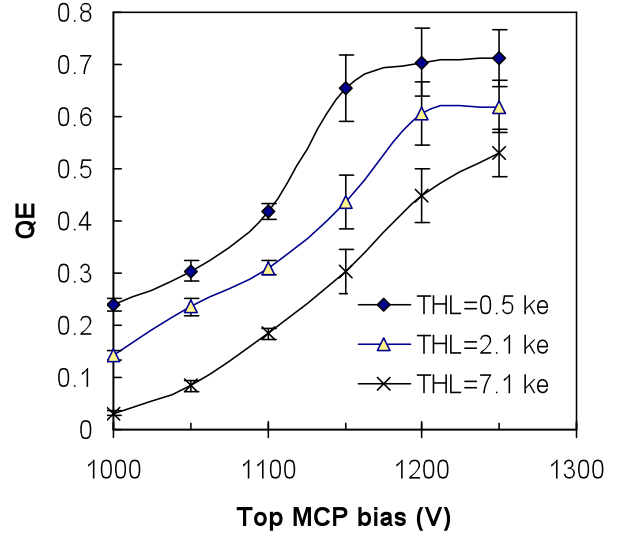


Fig. 3. Measured quantum detection efficiency of the MCP detector as a function of bias voltage applied to the neutron sensitive MCP. Legend indicates different levels of Timepix threshold. The amplifying MCP stack bias voltage was set to 1100V.

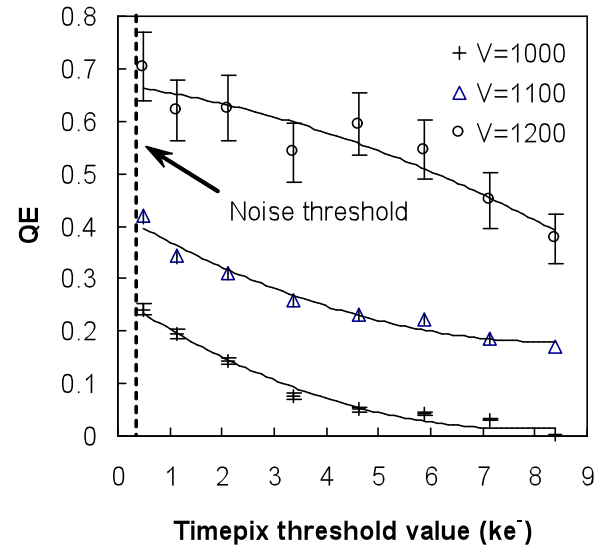


Fig. 4. Measured quantum detection efficiency of the MCP detector as a function of Timepix threshold setting. Legend indicates the neutron sensitive MCP voltage at which data was taken. The amplifying MCP stack is at 1100V bias.

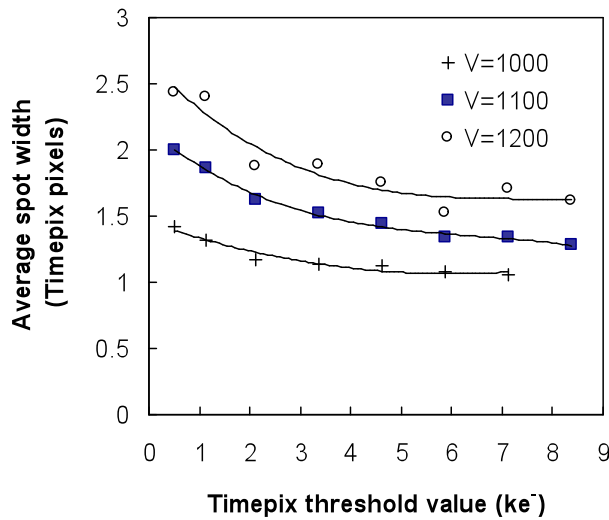


Fig. 5. Measured average spot size of event footprints as a function of Timepix threshold setting. Legend indicates the neutron sensitive MCP voltage at which data was taken. A compromise between the spatial resolution and the detection efficiency has to be found for a particular application.

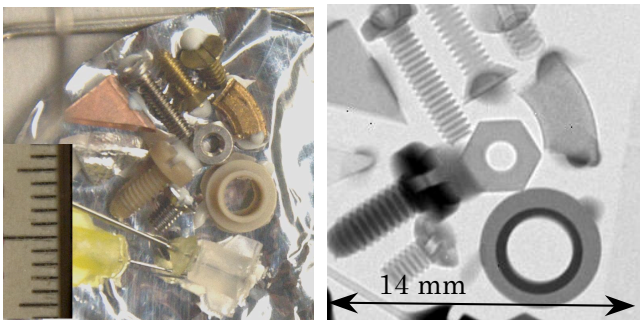


Fig. 6. The photograph and a neutron radiography of a test object consisting of metal and plastic objects obtained with new MCP-Timepix detector. The test objects contained steel screws and a nut, plastic washer and a screw, copper and brass pieces and steel needles. Field of view is 14 mm. Individual threads of the M2 screws are seen due to the high spatial resolution of the detector. Some edge enhancement is observed at the steel screws due to the neutron refraction.

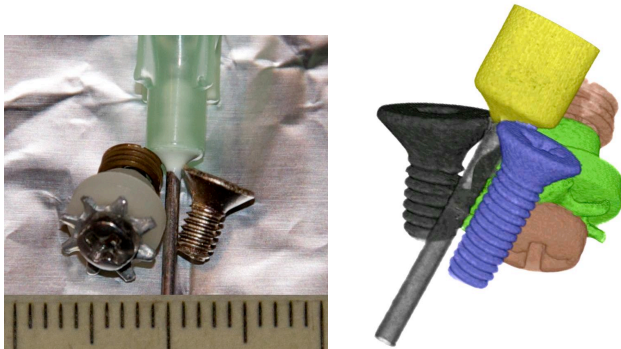


Fig. 7. Photograph and a neutron tomographic reconstruction of a test object obtained with the high-efficiency MCP-Timepix detector. High spatial resolution is achieved in tomographic reconstruction. Different types of M2 stainless steel screws could be separated by a slight variation in neutron absorption coefficient. Imaging was performed at FunSpin cold beam line of Paul Scherrer Institute. Full tomographic set was taken in ~30 minutes (202 projections, 8s exposure each).

Acknowledgment

This work was supported in part by the U.S. Department of Energy under STTR Grants No. DE-FG02-07ER86322 and DE-FG02-07ER86353 and National Science Foundation Grant No. DMR-0753599. The measurements reported here would not have been possible without the data acquisition boards and very effective software developed within the Medipix collaboration by our colleagues T. Holy, J. Jakubek, S. Pospisil et al. at the Institute of Experimental and Applied Physics, Czech Technical University in Prague [13], and the Muros readout electronics developed at NIKHEF [14]. This work was done within the Medipix collaboration.

References

- [1] D.S. Hussey, D.L. Jacobson, M. Arif, et al., Nucl. Instr. Meth. A 542 (2005) 9.
- [2] E. Calzada, B. Schillinger, F. Grunauer, Nucl. Instr. Meth. A 542 (2005) 38.
- [3] A. Hilger, N. Kardjilov, M. Strobl, et al., Physica B 385-86 (2006) 1213.
- [4] E. H. Lehmann, G. Frei, G. Kuhne, et al., Nucl. Instr. Meth. A 576 (2007) 389.
- [5] E.H. Lehmann, G. Frei, P. Vontobel, et al., Nucl. Instr. Meth. A 603 (2009) 429.
- [6] W. Kockelmann, G. Frei, E.H. Lehmann, P. Vontobel, J.R. Santisteban, Nucl. Instr. Meth. A 578 (2007) 421.
- [7] N. Kardjilov, A. Hilger, I. Manke, F. Garcia-Moreno, J. Banhart, Materials Testing 50 (2008) 569.
- [8] A.S. Tremsin, J.B. McPhate, W.A. Kockelmann, J.V. Vallerga, O.H.W. Siegmund, W. B. Feller, IEEE Trans. Nucl. Sci. 56 (2009) 2931.
- [9] A.S. Tremsin, J. B. McPhate, J. V. Vallerga, O. H. W. Siegmund, J. S. Hull, W. B. Feller, E. Lehmann, Nucl. Instr. Meth. A 604 (2009) 140.
- [10] A.S. Tremsin, W.B. Feller, R.G. Downing, Nucl. Instrum. Meth. A 539 (2005) 278.
- [11] A.S. Tremsin, J.B. McPhate, J.V. Vallerga, O.H.W. Siegmund, J.S. Hull, W.B. Feller, E. Lehmann, Nucl. Instr. Meth. A 605 (2009) 103.
- [12] X. Llopart, R. Ballabriga, M. Campbell, R. Dinapoli, et al., Nucl. Instr. Meth. A 581 (2007) 485.
- [13] T. Holy, J. Jakubek, S. Pospisil, et al., Nucl. Instr. Meth. A 563 (2006) 254.
- [14] D. San Segundo Bello, M. van Beuzekom, P. Jansweijer, H. Verkooijen, J. Visschers, Nucl. Instr. Meth. A 509 (2003) 164.